Research Article | Vol. 32, No. 27 / 30 Dec 2024 / Optics Express 48353
Optics EXPRESS

Rapid quench annealing of Er implanted Si for quantum networking applications

Mark A. Hughes,[1] Huan Liu,[2] Adam Brookfield,[3] Tianrui Wang,[4] Iain F. Crowe,[4,*] and Yaping Dan[2]

[1]School of Science, Engineering and Environment, University of Salford, Salford M5 4WT, UK
[2]University of Michigan-Shanghai Jiao Tong University Joint Institute, Shanghai Jiao Tong University, Shanghai 200240, China
[3]Department of Chemistry, University of Manchester, Oxford Road, Manchester M13 9PL, UK
[4]Photon Science Institute and Department of Electrical and Electronic Engineering, University of Manchester, Manchester M13 9PL, UK
*iain.crowe@manchester.ac.uk

Abstract: Erbium-implanted silicon (Er:Si) holds promise for quantum networking, but the formation of multiple Er centers poses a challenge. We show that the cubic center (Er-C) has C_{2v} or lower symmetry and propose all Er centers range between full Si- and full O-coordination. By co-implanting Si with Er and O (both 10^{19} cm^{-3}) and increasing the thermal anneal quenching rate from ~100 °C/s to ~1000 °C/s, we shifted the dominant optically active center from Er_2O_3 clusters to the Er-C center with mixed Si and O coordination. Temperature-dependent photoluminescence reveals Er_2O_3 clusters and Er-C centers have O-related defect states at ~200 and 90 meV above the $^4I_{13/2}$ Er manifold, respectively.

1. Introduction

The transmission of quantum information using photons at 1550 nm has many applications in quantum networking. For quantum key distribution, a quantum repeater is required, and entanglement swapping based quantum repeaters require a quantum memory. Atomic vapors and color centers in diamond have been proposed for quantum memory applications, but atomic vapors aren't easily integrated with optical fibre or photonic waveguides, and have issues with atomic motions causing photon loss, while diamond color centers necessitate a challenging conversion to telecoms wavelengths. The tendency of rare earths (REs) to have relatively large inhomogeneous linewidths and relatively narrow homogeneous linewidth makes them suitable for quantum memory protocols that involve spectral hole burning techniques. A notable protocol is Gradient Echo Memory (GEM) which uses a varying electric field, parallel to the photon propagation direction, applied to a high optical depth RE ensemble with a narrow "burnt in" absorption band. In principle, GEM efficiencies can reach ~100%, and it boasts the highest reported storage efficiency for a RE quantum memory of 69% using free space Pr:Y_2SiO_5 [1].

With Er:Si, we can take advantage of well-established Si integrated circuit (IC) fabrication methods, as well as the well-established, highly repeatable and scalable networks that can be obtained using Si photonics, and the ability to integrate or interface with other Si based quantum computing platforms, such as donor, quantum dot, superconducting or photonic. A number of recent advances have been made in Er:Si, including Er implanted Si waveguides with a homogeneous linewidth of 9 kHz by Gritsch *et al* [2], our own reported spin T_2 time ~10 µs in Er implanted ^{nat}Si [3], which has now been extended to the ~ms range in Er implanted ^{28}Si [4], spin-resolved excitation of single Er centers with <0.1 GHz spectral diffusion linewidth [5], and our report of the first coupling with superconducting circuits [6].

#540726 https://doi.org/10.1364/OE.540726
Journal © 2024 Received 30 Aug 2024; revised 25 Oct 2024; accepted 26 Oct 2024; published 19 Dec 2024

Optics EXPRESS

An Er:Si waveguide based GEM memory could potentially improve efficiency over Er doped transparent bulk crystals by having uniform mode confinement along the beam propagation axis and precise control of the E-field gradient from the ability to precisely pattern electrodes on Si. This same quantum memory could be used in photonic quantum computers for synchronisation.

When Er is implanted into Si, co-implantation or doping with another impurity, usually O, is required to observe strong luminescence by indirect, above bandgap, excitation, along with narrow EPR lines and n-type conductivity. At least six different spin centers have been identified by EPR [7,8], along with numerous different luminescence centers, depending on the processing conditions [2,9–11]. The ~100s nm optical path length of Er implanted Si substrates did not allow direct (resonant) excitation of Er until Gritsch *et al* observed directed excitation from Er:Si photonic waveguides (~mm optical path length) [2]. Although no co-doping was used, four Er emitting centers were observed. Arguably, the main issues with Er:Si are the number of different centers formed, the ability to control which centers are formed and an understanding of what those centers are. In order to fully realize the potential of Er:Si, the formation of these centers needs better control. It should be noted that sublimation molecular beam epitaxy (SMBE) can be used to produce Er doped Si with a single Er center observed by indirect excitation, which is distinct from Er centers produced by implantation [10]. Here we focus on implantation because of its superior compatibility with the silicon fabrication techniques that could be used to fabricate Er:Si quantum networking devices.

We have recently developed a 'deep cooling' process that follows thermal annealing. This involves using cryogenically cooled He gas to increase the post annealing quench rate by around an order of magnitude, compared to conventional rapid thermal annealing (RTA) and standard cooling cycles. We have previously used high concentrations of $7.5 \times 10^{20}\,\mathrm{cm}^{-3}$ Er and $2 \times 10^{21}\,\mathrm{cm}^{-3}$ O implanted Si combined with our 'deep cooling' process, to demonstrate reduced Er clustering and intense room temperature (RT) luminescence with above bandgap excitation, which has a variety of photonic applications [12,13]. We have also observed strong RT electroluminescence [12,14] and stimulated emission [15] from Er and O implanted Si LEDs, processed with 'deep cooling'. However, all our previous work on 'deep cooling' of Er/O implanted Si didn't have well resolved crystal field peaks due to the high Er and O concentrations used.

Here we apply the 'deep cooling' process to Si samples with much lower Er concentrations that are more applicable to quantum networking applications and by resolving crystal field splitting we show that the various Er centers can be represented on a sequence from entirely Si coordinated, through mixed O and Si coordination, to entirely O coordinated, with O coordination being energetically favorable. We show that in Er and O co-implanted Si, our 'deep cooling' technique can push the coordination towards greater Si coordination, which could be used in Er only implantation to obtain a single Si coordinated Er center, which is essential for quantum networking applications of Er:Si.

2. Experimental

2.1. Sample fabrication

Intrinsic (100) Si wafer, 500 μm thickness, supplied by Sigma-Aldrich, with a measured resistivity of 5.5 kΩcm was implanted with a chain of isotope specific ^{167}Er implants up to 1.5 MeV and O up to 200 keV to give a flat concentration profile of $\sim 10^{19}\,\mathrm{cm}^{-3}$ for Er and O down to a depth of ~500 nm, see Supplement 1 section S1. We chose this recipe because it has been shown by varying Er and O concentrations, that optimum luminescence intensity can be obtained from Er and O co-implanted silicon-on-insulator (SOI), with $10^{19}\,\mathrm{cm}^{-3}$ Er and $10^{19}\,\mathrm{cm}^{-3}$ O [16].

Annealing was carried out in a RTA, which had a peak cooling rate of ~100 °C/s, at 700 °C, 800 °C, 900 °C and 950 °C for 10 min, samples referred to as RTA 700, RTA 800, RTA 900, RTA 950, respectively and using 'deep cooling' (DC) at 900 °C and 950 °C for 10 min, samples

Optics EXPRESS

referred to as DC 900 and DC 950, respectively. In order to perform 'deep cooling', we used a modified dilatometer (DIL 805A, TA Instruments), in which the samples, with a maximum width of 3 mm, were annealed at 900 °C and 950 °C for 10 min by induction heating at a pressure of 5×10^{-4} mbar, followed by flushing with high-purity He (99.999%) gas cooled in LN2 (77 K) giving a peak cooling rate of ~1000 °C/s. A K-type thermocouple was used to monitor the temperature, which was controlled by adjusting the He flow rate.

Photoluminescence (PL) spectra were obtained by placing the samples in a closed cycle He cryostat with a base temperature of 3.5 K. Samples were excited with a 450 nm, 50 mW laser diode powered by a laser diode driver that was electronically amplitude modulated by a function generator to give an overall fall time of ~1 µs. The PL was dispersed in a Bentham TMc300 monochromator and detected with an infra-red (IR) sensitive photomultiplier tube (PMT) and the signal was recovered with a SR830 lock-in amplifier. Transient PL measurements were taken using the same system used for spectral measurements, except the transient signal was captured with an oscilloscope with a 500 MHz bandwidth.

EPR measurements were taken on a Bruker EMX EPR spectrometer at a temperature of 5 K, with the magnetic field approximately parallel to the [110] crystal axis of the samples. The field modulation was 100 kHz, and the microwave frequency was 9.37 GHz. Raman measurements were performed on a Horiba labRAM evolution confocal Raman microscope with 488 or 633 nm laser excitation. Electrical conductivity measurements were carried out using a standard four-point probe.

2.2. Crystal field analysis

The Hamiltonian (H) of Er^{3+} can be described as:

$$H = H_F + H_{CF} + H_{Ze} \tag{1}$$

where H_{CF} describes the electric field produced by the environment of the host crystal lattice surrounding the Er^{3+} ion, and is given by the linear combination of spherical tensors of various ranks, $C_q^{(k)}$, and crystal field parameters (CFPs), B_q^k, as shown in Eq. (2):

$$H_{CF} = \sum_{k,q} B_q^k C_q^{(k)} \tag{2}$$

Only rank $k = 2$, 4 and 6 are allowed, with q taking values of 0 to k, and taking into account the imaginary $C_q^{(k)}$, for $q > 0$, gives a total of 27 $C_q^{(k)}$ and associated B_q^k CFPs. Each crystallographic point group has its own set of CFPs [17]. Details of the construction of H_{CF} are given elsewhere [18]. Each $^{2S+1}L_J$ manifold will have its own H_{CF} and the crystal field splitting is given by the eigenvalues of H_{CF}. To determine CFPs from experimentally derived crystal field splitting we used a least square algorithm that varied the B_q^k values to minimize the difference between the observed splitting and the eigenvalues of H_{CF}.

H_F accounts for the interactions that occur in a free RE ion. Each RE has its own set of H_F parameters, and these vary little between hosts. For the fitting process, we didn't take into account H_F but we used the H_F parameters given by Carnall *et al.* for Er:LaF_3 [19] to calculate the absolute energy of excited state manifolds.

In Kramers-type REs, such as Er, with low symmetry, the crystal field splits each $^{2S+1}L_J$ manifold into J+½ degenerate crystal field doublets. The Zeeman interaction, H_{Ze}, which splits these doublets in a magnetic field is given in Eq. (3):

$$H_{Ze} = g_J \mu_B \boldsymbol{J}.\boldsymbol{H} \tag{3}$$

where g_J is the Landé factor, μ_B is the Bohr magneton, $\boldsymbol{J}$ is the angular momentum operator, and $\boldsymbol{H}$ is the magnetic field strength [20]. H_{Ze} is not considered in our crystal field fitting procedure.

Optics EXPRESS

2.3. EPR g tensor calculation

There are two sets of eigenvectors for each degenerate crystal field doublet: $|+\rangle$ and $|-\rangle$. The First order perturbation equations in Eq. (4) are used to determine the diagonal components of the g tensor, g_x, g_y, and g_z [20].

$$g_x = 2g_J \langle +|\boldsymbol{J}_x|-\rangle \,,\; g_y = 2g_J \left\langle +|\boldsymbol{J}_y|-\right\rangle \,,\; g_z = 2g_J \langle +|\boldsymbol{J}_z|+\rangle \tag{4}$$

where $\boldsymbol{J}_x$, $\boldsymbol{J}_y$, $\boldsymbol{J}_z$ are the vector components of $\boldsymbol{J}$ such that $\boldsymbol{J}^2 = \boldsymbol{J}_x^2 + \boldsymbol{J}_y^2 + \boldsymbol{J}_z^2$.

3. Results and discussion

3.1. Photoluminescence

Figure 1(a) shows the normalized PL spectra of the DC 950 sample at different modulation frequencies, measured at 3.5 K. Approximately fourteen relatively narrow peaks are identified, all with FWHM ~20 cm^{-1}, which is more than the maximum of eight peaks that could result from a single Er center, indicating that the PL must originate from more than one Er center. Using the fact that different Er centers could have different lifetimes, we increase the laser modulation frequency to reduce the PL intensity. In the ratio of low to high modulation frequency spectra, negative peaks correspond to peaks with shorter lifetimes. Using this technique, we can distinguish PL peaks arising from two different centers: a short lifetime center (black arrows) and a long lifetime center (red arrows). In the short and long lifetime centers the PL intensity decreased by a factor of ~4 and ~5, respectively, indicating that their difference in lifetime is only ~20%. In Fig. 1(b), we used the same technique but increased the temperature to 65 K; at this increased temperature, two peaks emerge on the short wavelength (higher energy) side of the most intense peak. These can be attributed to transitions from the first two thermally excited crystal field levels of the $^4I_{13/2}$ manifold to the lowest crystal field level of the $^4I_{15/2}$ ground state manifold (hot lines).

Figure 1(c) shows the PL spectrum of the RTA 950 sample. Even though this sample was part of the same implanted wafer and had the same annealing temperature and time as the DC 950 sample, the PL spectra are markedly different: peaks are broader and less discernible than in DC 950, and the peaks that can be observed are at different wavelengths. The normalized spectra of the low and high modulation frequency are almost identical, as evidenced by the almost featureless spectrum of the ratio of these modulation frequencies. This suggests that all the peaks from RTA 950 are from the same Er center. Integrated PL intensity was ~2× larger in DC 950 compared to RTA 950.

Figure 1(d) shows the 3.5 K and 65 K spectra of the RTA 950 sample, with main peaks at 6501 cm^{-1} and 6510 cm^{-1}, respectively; this thermally induced shift in peak position did not occur in DC 950. Thermal broadening of the emission peaks was also more apparent in RTA 950, than for DC 950. The intensity of the peak at 6476 cm^{-1}, marked HL3, increases with temperature, indicating that it is also a hot line. We have previously observed a hot line at 6472 cm^{-1} in high concentration Er and O implanted Si, treated with our 'deep cooling' process [13]. Hot lines on the high energy side of the main peak can't be clearly observed due to thermal broadening of the most intense emission peak at 65 K, so to identify them we took the 2nd derivative of the PL spectrum, which can be used to enhance spectral resolution; in this case, emission lines correspond to negative peaks, i.e., for $d^2I/d\lambda^2 < 0$, [21,22]. This procedure reveals a separate hot line (HL1) at 6538 cm^{-1}.

As can be seen in Supplement 1 Fig. S2 a), the spectral position of emission lines in the PL of DC 900 and DC 950 are identical, although for DC 900 the short lifetime center peaks are relatively weaker, and the long lifetime peaks relatively stronger than DC 950. Similarly, Supplement 1 Fig. S1 b) shows that the RTA 900 and RTA 950 samples also have very similar spectra. This indicates that differences in the PL spectra between the DC and RTA samples are

Optics EXPRESS

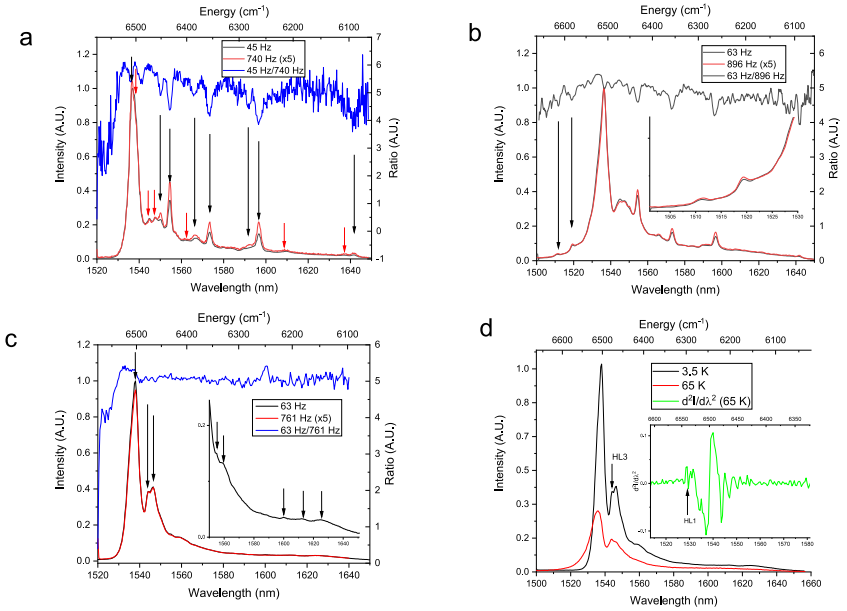

Fig. 1. (a) Normalized PL from DC 950 at 3.5 K at slow and fast modulation frequencies, along with the ratio of slow to fast modulation spectra. (b) Normalized PL from DC 950 at 65 K at slow and fast modulation frequencies, along with the ratio of slow to fast modulation spectra. Inset shows a closeup of the hot lines. (c) Normalized PL from RTA 950 at 3.5 K at slow and fast modulation frequencies, along with the ratio of slow to fast modulation spectra. Inset shows a closeup of the long wavelength region. (d) PL from RTA 950 at 3.5 and 65 K, a hot line (HL3) is indicated. Inset shows the 2nd derivative of the 65 K PL to resolve the first hot line (HL1), as indicated by the arrow.

due to the quenching rate, rather than any possible differences in the annealing temperatures of the two samples. In both DC and RTA samples, the integrated PL intensity was ~2× higher for the 900 °C anneal than for the 950 °C anneal. Raman measurements in Supplement 1 section S3 show that when annealing at temperatures of 700 and 800 °C by RTA, some residual amorphization and strain is evident, but when annealing at or above 900 °C (for both RTA and DC samples) no such residual amorphization or strain was evident.

3.2. *Inconsistencies of the cubic center assignment*

In early work on Er:Si, Tang *et al*. reported a PL spectrum with five peaks when annealing at 900 °C for 30 min. These were attributed to a cubic (Er-C) center on the basis that five peaks would be expected from an Er center with cubic symmetry [23]. More peaks where observed with lower temperature anneals, which was attributed to the presence of a non-cubic Er center [18]. In later, more extensive work, Przybylinska *et al*. observed the same five peaks of the cubic center along with its first two hot lines in Er implanted float zone (FZ) Si, and the appearance of additional peaks in samples with higher O concentrations, which was attributed to the presence of non-cubic, O-coordinated centers [9]. If we compare the peak positions of our DC 950 short lifetime (DC 950 SL) center to Er-C, as can be seen on the left side of Fig. 2, the most prominent PL peaks from our DC 950 SL peaks and the hot lines match very closely with Er-C (denoted 'Przybylinska Cubic'). There are three weak satellite peaks in the $^4I_{15/2}$ manifold of the DC 950 SL spectrum, which gives the total of eight peaks expected for a low symmetry site, that were not previously reported for Er-C. On the righthand side of Fig. 2, we also show the peaks from our

Optics EXPRESS

RTA 950 sample, compared with our DC 950 long lifetime (DC 950 LL) spectrum and those from RTA 950, which shows that the first four DC 950 LL CF levels match those in RTA 950, indicating that the DC 950 LL peaks represent the remnant of the remaining RTA 950 center.

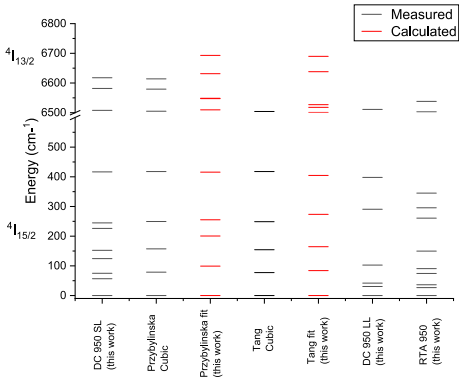

Fig. 2. Crystal field splitting of our RTA 950 and DC 950 samples, compared with supposed cubic crystal field splitting from the literature, Przbylinska [9] and Tang [23].

If we examine the literature on Er:Si PL, the same five PL lines can be seen; however, the same satellite peaks that we observe in DC 950 SL can also be observed, but were not commented on [11,24–29]. A wide variety of implantation and annealing conditions were used in these studies, yet all produce the same characteristic peaks.

A cubic center can be fitted with four CFPs, two of which have a constant ratio to the other two, giving two adjustable parameters to describe the cubic crystal field. These two CFPs can be re-expressed so that relative splitting is described by a single parameter, x, and a linear scaling factor, W, which can be thought of as a stretch of the splitting, determined by x [30].

The irreducible representations, Γ, of the cubic group give the crystal field levels. As shown in Fig. 3, in a cubic field the $^4I_{15/2}$ manifold splits into two Kramers doublets (Γ_6 and Γ_7) and three Γ_8 quartets. A $\Gamma_a \rightarrow \Gamma_b$ transition is subject to selection rules: the transition is allowed if the reduction of $\Gamma_K \otimes \Gamma_b$ contains Γ_a, in cubic symmetry, $\Gamma_K = \Gamma_5$ [31]. This results in $\Gamma_6 \rightarrow \Gamma_6$ and $\Gamma_7 \rightarrow \Gamma_7$ transitions being forbidden.

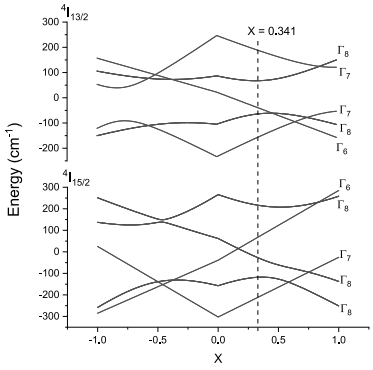

Fig. 3. Cubic crystal field splitting for $^4I_{15/2}$ and $^4I_{13/2}$ manifolds.

Cubic CFPs have previously been fitted to the $^4I_{15/2}$ splitting of the Er-C center [9,32]. We have also carried out the fitting of the splitting reported by Tang [23] here, see Fig. 2, and find similar fitting parameters (x = 0.341, W = 0.970) with a root mean square deviation (RMSD) = 30.5 cm^{-1}.

Optics EXPRESS

However, the predicted splitting of the $^4I_{13/2}$ manifold has no match to the observed hot lines. Also, given the selection rules, this presents a problem for the fit with x = 0.341, since Γ_7 is the ground state of the $^4I_{13/2}$ manifold, so only four transitions to the $^4I_{15/2}$ manifold are allowed. In fact, for all five transitions to be allowed, Γ_8 needs to be the ground state of the $^4I_{13/2}$ manifold, which only occurs for -1 < x < -0.4, but the splitting in this x range does not match the spectrum of Er-C. One possibility is that x is actually at the cross-over of Γ_6 and Γ_7 in the $^4I_{13/2}$ manifold at x = 0.65, because of the range of crystal field sites giving a range of x values for the Er-C center there could be transitions from both Γ_6 and Γ_7 so all five transition could be observed. The problem with this is that small changes in the crystal field that could be expected for different processing conditions would change x slightly. This would change which transitions are observed, but the peaks of the Er-C center are very stable and reproducible, the fit to the $^4I_{15/2}$ splitting is made significantly worse (RMSD = 82 cm^{-1}) and the splitting of the $^4I_{13/2}$ manifold cannot explain the observed hot lines. In fact, if we attempt to fit all the known splitting of Er-C ($^4I_{15/2}$ PL and $^4I_{13/2}$ hot lines), there is no acceptable fit to cubic CFPs. We can have a high confidence in the null fit result precisely because the peaks of the Er-C center are so stable and reproducible, and there are only two degrees of freedom for the cubic fit, so it is relatively easy to search the entire parameter space. Along with the consistent observation of three satellite peaks and the fact that five peaks can only be observed for a very limited set of cubic crystal fields, this leads us to propose with confidence that Er-C is not, in fact, a cubic center; however, for consistency with the literature we refer to this center as Er-C.

3.3. Crystal field analysis

Crystal field analysis is a powerful tool in determining which RE centers are present from their optical spectra. Typically, this is done with RE doped transparent bulk crystals which allows observation of the stark splitting of many manifolds, by absorption measurements, giving, perhaps, hundreds of experimental energy levels to fit both crystal field and free ion parameters. For Er:Si, much more care must be taken in performing and interpreting crystal field analysis since, from indirect PL measurements, we only have the splitting of the $^4I_{15/2}$ manifold, plus a few (hot line) levels from the $^4I_{13/2}$ manifold. More recently, the complete $^4I_{13/2}$ splitting of a few Er centers from direct PL of Er:Si waveguides [2] and optically modulated magnetic resonance (OMMR) [33] were added. The significance of a good fit to a single manifold should be downplayed, especially considering the previous confusion over a cubic fit to the Er-C center. Here, we use the many centers observed in Er:Si to our advantage by assuming that all, or at least a subset, of these centers can be placed in a sequence that represents some monotonic change in their local environment. A monotonic change in local environment, such as a shift in primitive cell dimension or shift in coordination from Si to O, for example, would be expected to give a monotonic shift in fitted CFPs [18]. To put the centers in a sequence we look for trends in their splitting, and then look for trends in the fitted CFPs, which would be expected for a monotonic change in local environment. This effectively gives more data points for the analysis and validates one fit against another. We also calculate g-factors from the fits and compare to EPR and Zeeman measurements for further validations.

In order to determine which symmetry group CFPs to fit, we can employ a descending symmetries technique [34]. Starting with the cubic O_h symmetry of the Si host, which is ruled out with a high degree of confidence, the eight lines observed in the Er-C $^4I_{15/2}$ manifold means it must have tetragonal or lower symmetry. The next lowest symmetry progressing down the symmetry subgroups [35] is tetragonal D_{2d} [18]; however, no good fit for the DC 950 SL lines could be found for tetragonal CFPs. The main issue is the large separation of the first two crystal field levels in the $^4I_{13/2}$ manifold. Since tetragonal symmetry is a distortion of cubic symmetry, unless the tetragonal distortion is very large, there will be a lot of similarity to the splitting seen in Fig. 3. We attempted to fit hexagonal and trigonal CFPs, which were not as good as

Optics EXPRESS

orthorhombic, ruling out the hexagonal branch, or the crystallographic subgroups. The next lowest symmetry in this series is orthorhombic C_{2v} symmetry, which has nine CFPs and is often employed for the crystal field analysis in situations where the symmetry is uncertain [34]. With this number of degrees of freedom in the fit, care must be taken to avoid local minima, so we randomly adjusted starting parameters to help find the global minimum. An additional issue is that there could be unresolved peaks, or peaks from a different center in any spectrum, although our method of arranging spectra in a sequence should help identify the presence of any such peaks.

From the first resonant excitation of Er:Si waveguides, Gritsch *et al* identified sites A, B, P and O [2]. Sites A and B are of particular interest since they have not been observed before. Site P was attributed to precipitates and site O was attributed to an indirectly excitable center. The Gritsch A and B centers are consistent with our previous indirect measurement of the $^4I_{13/2}$ splitting using OMMR [33], see Supplement 1 section S4.

The measured splitting of Gritsch site A and B, and DC 950 SL can be arranged in a sequence, as shown in Fig. 4, along with the fitting of these with orthorhombic CFPs. All of these were reasonably well reproduced, with Gritsch site A being a particularly good fit. Measured Gritsch sites A and B exhibited only six levels in the $^4I_{15/2}$ manifold, which could be due to the long wavelength cutoff of the detection system used in their experiments. By allowing two levels in the $^4I_{15/2}$ to vary freely, the fits predict the position of the two longest wavelength PL peaks. Our proposed RTA 950 crystal field splitting is also shown. The first excited Stark level of the $^4I_{13/2}$ manifold was determined from the 2nd derivative of the 65 K PL spectrum in Fig. 1(d) and corresponds to hot line, HL1. The hot line, HL2 transition would approximately overlap with the main PL peak, which explains why it was not observed, and could explain the shift and excessive thermal broadening of the main PL peak, as shown in Fig. 1(d). The hot line, HL3 transition corresponds to the 6476 cm^{-1} peak in Fig. 1(d), and is consistent with hot line, HL1.

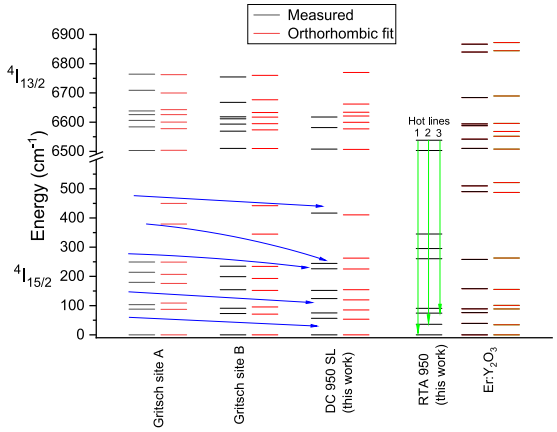

Fig. 4. Measured crystal field splitting and orthorhombic fit to Gritsch site A and B [2] DC 950 SL, RTA 950 (this work) and Er:Y_2O_3 [37]. Blue arrows indicate the trend in monotonic shift, green arrows indicate the proposed hot line transitions for RTA 950 (HL1,2,3). See Supplement 1 Table S1 for values.

The RTA 950 splitting could not be put in the same sequence as the Gritsch A, B and DC 950 SL levels, but it does closely match the Stark splitting of Er_2O_3 [36], which has an almost identical splitting to Er doped Y_2O_3 [37] in C_2 sites, and in both of these materials, Er is 6 fold coordinated to O. The missing level at ~155 cm^{-1} may not have been resolved because of inadequate spectral resolution. Additional peaks at 295 and 345 cm^{-1} can be attributed to Er in different sites, which was also observed in Er doped Y_2O_3 [37]. Because of the strong similarity,

Optics EXPRESS

we propose that the emission peaks in the RTA 950 spectrum originate from the same six-fold O coordinated Er center, with C_2 symmetry as that observed in Er_2O_3 and Er:Y_2O_3. The splitting of Er:Y_2O_3 was previously fitted to the 14 CFPs of the C_2 point group [37], but for consistency with our fitting to Gritsch A, B and DC 950, we fitted with the 9 CFPs of C_{2v}, of which C_2 is a subgroup.

Figure 5 shows the orthorhombic CFPs from the fits shown in Fig. 4. Since the C_{2v} symmetry can be thought of as an orthorhombic distortion to a tetragonal C_{4v} field, we separate the C_{2v} CFPs that are common to C_{4v}. Figure 5 shows a near-monotonic trend in all CFPs for the sequence Gritsch A, B and DC 950, as would be expected for a monotonic shift in local environment. It also shows that the C_{2v} fit to Er:Y_2O_3, and by extension RTA 950, does not follow the same sequence.

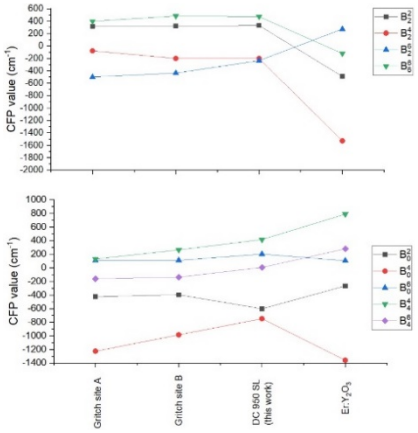

Fig. 5. C_{2v} Orthorhombic CFPs from fits shown in Fig. 4. The bottom panel shows the CFPs common to C_{4v} symmetry, whereas the top panel shows those unique to C_{2v} symmetry. See Supplement 1 Table S2 for values.

The RTA 950 center is the six-fold O coordinated Er center in Er_2O_3. However, in order to form this center, an O:Er ratio of ~6 is required, but RTA 950 only has an O:Er ~1. It is possible for O to diffuse to the surface during annealing, but this would be limited a depth of ~10 µm [38–40]. Given the background O concentration of our FZ wafer is $\sim 10^{15}\,cm^{-3}$, the amount of diffused O available is at most $\sim 10^{12}\,cm^{-2}$, compared with the implanted Er dose of $4.18 \times 10^{14}\,cm^{-2}$. So, either ~1/6 of the implanted Er is used to form individual six-fold O coordinated Er centers, or ~2/3 of the implanted Er is used to form Er_2O_3 clusters. Er_2O_3 cluster formation is the more likely explanation, otherwise we would have to explain why the remaining 5/6 of the implanted Er formed some indirect excitation inactive center, such as Gritsch A and B, rather than Er-C, which is readily formed in Er:Si.

3.4. Comparison to EXAFS

A range of Er PL centers associated with co-doping with O [9,11,41] that are yet to be classified in our sequence in Fig. 4 are referred to as "unclassified". Extended X-ray absorption fine structure (EXAFS) measurements have been performed on Er:Si samples with a range of implantation and annealing conditions. These are summarized in Table 1, along with the PL assignment from those, or similar, Er:Si samples. We can put the reported coordination of Er in a sequence: Si only coordination (12- or 6-fold), mixed Si and O coordination, O only coordination (4- to 6-fold). In the associated PL assignment column, we identify both the characteristic Er-C center, along with those categorized as "unclassified". This associated PL can be summarized as: very weak

Optics EXPRESS

Er-C PL from Si only coordination, clear, strong Er-C PL from mixed Si and O coordination and mixed Er-C and "unclassified" PL from O only coordination. We propose that the Er-C center has mixed coordination, the Gritsch A and B centers have entirely, or close to entirely, Si coordination. The reason Gritsch A and B centers are not observed by indirect excitation is because the O is needed to create a defect level to allow indirect excitation. The Er_2O_3 clusters in RTA 950, and the as yet unclassified Er:Si PL [9,33,41] have 4- to 6-fold O coordination.

Table 1. Summary of Er:Si EXAFS measurements and their associated PL assignment from the literature[a]

O coord.	Si coord.	Implant	Anneal	Ref.	PL
5.5	-	10^{19} Er, 10^{20} O (CZ)	900 °C 12 hr	[42]	[c]
5.9	-	10^{19} Er, 10^{20} O (CZ)	900 °C, 30s	[42]	[b]Unclassified (10^{19} Er, 10^{20} O; 900 °C, 30s [43])
	12	5×10^{17} Er (FZ)	927 °C, 30 min	[44]	[b]Er-C v weak (5×10^{17} Er; 900 °C 30 min [9])
6		5×10^{17} Er (FZ)	927 °C, 30 min	[44]	
3	6	10^{19} Er, 3×10^{19} O	[a], 900 °C, 30 s	[45]	Er-C + weak unclassified
5.1 ± 0.5	-	10^{19} Er, 10^{20} O	[a], 900 °C, 30 s	[45]	Er-C + unclassified
4 ± 1	-	10^{19} Er, 10^{20} O	[a], 900 °C, 12 hr	[45]	Unclear
	6 ± 2	10^{19} Er, 10^{20} O	450 °C, 30 min	[46]	Unclear
3 ± 2	4.4 ± 0.6	10^{19} Er, 10^{20} O	[a]	[46]	Er-C + unclassified
5.1 ± 0.5		10^{19} Er, 10^{20} O	[a], 900 °C, 30 s	[46]	Er-C + unclassified
5.0 ± 0.5		10^{19} Er, 10^{20} O	[a], 900 °C, 12 hr	[46]	Unclear

[a]In the "Implant" column, the wafer type is provided in parentheses; if not, it was not reported. [a] is shorthand for 450 °C for 30 min, 620 °C for 3 hr. [b] If PL wasn't reported in the EXAFS publication, the PL center and processing conditions from the most similar sample in the literature are provided. [c]No good match found in literature. "Unclear" means that the PL spectrum was too featureless or noisy to identify a PL center.

The associated PL can be explained by the sensitivity limit of EXAFS: the 12 Si only coordination FZ sample has very weak Er-C PL because only a few Er-C centers, below the EXAFS sensitivity limit, can be formed from the residual O impurities in FZ Si. The majority of the Er is Si only coordinated, the PL for which is only activated by direct (resonant) excitation. Similarly, for the O only coordinated Er, which has mixed Er-C and unclassified PL emission lines, a fraction of Er has the mixed Er-C coordination, while the majority has the O only, unclassified Er centers. Both EXAFS measurements [44] and DFT calculations [47] indicated the preference for Er to coordinate with O impurities over Si, which suggests that O coordination is energetically favorable to Si. We propose that the reason 'deep cooling' reduces O coordination is that at the annealing temperatures used, O coordination is less energetically favorable and, during annealing the Er is preferentially coordinated with Si. With a slow quench there is sufficient time at lower temperatures (where atomic rearrangement can still occur, but O coordination is favorable) for the higher O coordinated Er centers to form, whereas with a rapid quench there is insufficient time for Er to coordinate with O. This proposed mechanism has analogies to the quenching of a molten glass, where a rapid quench can form the less energetically favorable amorphous state, and a slow quench can form the more energetically favorable crystalline state. The proposed Er centers are summarized in Table 2, a notable center is the Er-1 center observed in Er doped Si fabricated using SMBE, Er-1 was found to have C_{2v} symmetry from Zeeman measurements and a proposed mixed Si and O coordination, [10] we have included Er-1 in Table 2. It should be noted that Gritsch A and B centers were not observed in Er implanted SOI when implanted at temperatures over 600 °C [48]. We explain this as being cause by diffusion of O from the buried SiO_2 layer at higher implant temperatures which causes higher O coordination of Er.

Optics EXPRESS

Table 2. Summary of proposed centers formed in Er implanted Si

Center	O coordination	Si coordination	Symmetry	PL excitation	Energetic favorability
Gritsch A	0	6-12	C_{2v}, or lower	Resonant only	Least
Gritsch B	1-2	6-12	C_{2v}, or lower	Resonant only	
Er-C	2-6	2-6	C_{2v}, or lower	[a]	
Er-1	2-6	2-6	C_{2v}	[a]	
Unclassified	4-6	0-2	unknown	[a]	
RTA 950	6	0	C_{2v}, or lower	[a]	Most

[a]Indirect via O-related defect state

3.5. *g-factor calculation*

In Er:Si, particular processing conditions are required to obtain EPR active centers. Supplement 1 section S6 shows that no EPR signal could be obtained for DC 950, whereas for $10^{19}\,cm^{-3}$ Er and $10^{20}\,cm^{-3}$ O, a strong EPR signal is observed. If an EPR signal cannot be measured from optically active Er:Si, given a sensitive enough method, Zeeman measurements can still be performed. Yang *et al* used Zeeman measurements from a $10^{17}\,cm^{-3}$ ^{167}Er and $10^{18}\,cm^{-3}$ O co-implanted FinFET transistor, annealed at 700 °C, to obtain the g-tensor, hyperfine A-tensor, and their associated Euler angles for the CF ground states of the $^4I_{15/2}$ and $^4I_{13/2}$ manifolds.

In Table 3 we show the principal values of the g-tensors calculated from the CFPs obtained from our fitting. There is a very good agreement between both the $^4I_{15/2}$ and $^4I_{13/2}$ calculated g-tensors of the Gritsch B center and those measured by Yang. There is also good agreement between the g-tensor calculated from our C_{2v} fit to Er:Y_2O_3 and the OEr-3 center, derived from EPR by Carey et al [49]. We can accurately predict the measured g-factor of Er:Y_2O_3 from our C_{2v} fit to its Stark levels, which serves as a good test case of our method.

Table 3. g-tensors calculated from the CFPs in Fig. 5 along with g-tensors measured by Zeeman [50] and EPR [49]

Center	g-tensor						Symmetry	Ref
	$^4I_{15/2}$			$^4I_{13/2}$				
	g_x	g_y	g_z	g_x	g_y	g_z		
	Calculated							
Gritsch A	0.40	1.36	16.36	0.16	0.33	14.06	C_{2V}	This work
Gritsch B	0.72	2.91	14.98	0.32	0.70	13.75	C_{2V}	This work
Er-C	1.49	3.04	14.80	0.38	0.48	13.99	C_{2V}	This work
Er:Y_2O_3	1.02	3.96	11.83	0.86	1.14	12.61	C_{2v}	This work
	Measured							
Yang	0.55 ± 0.19	2.38 ± 0.18	14.846 ± 0.028	0.16 ± 0.16	0.59 ± 0.17	13.1 ± 0.023	C_1	Zeeman [50]
Carey OEr-3	1.09	5.05	12.78				C_1	EPR [49]
Er:Y_2O_3	1.645	4.892	12.314				C_2	EPR [51]

Yang *et al* concluded their Er center had monoclinic C_1 symmetry based on misalignment between the $^4I_{15/2}$ and $^4I_{13/2}$ g-tensors. This is consistent with our finding of C_{2V} symmetry since our method of descending symmetries will give the highest symmetry capable of reasonably explaining the observed splitting added to the fact that C_1 symmetry is obtained by applying a distortion to C_{2V} symmetry.

Optics EXPRESS

3.6. Indirect excitation mechanism

The indirect excitation mechanism for Er:Si is thought to involve transfer of energy, from excitons generated by above bandgap excitation, to the optically active Er site, via an intermediate defect state associated with the presence of an Er-O center in the Si lattice, which lies below the bottom of the conduction band by and energy E_{DT}. Quenching of the excited Er is thought to occur either by Auger quenching (via impurity-Auger and/or exciton-electron-Auger recombination) [25], with an associated activation energy E_{AQ}, or by a back-transfer process that involves phonon assisted transfer from an excited Er to an Er-O defect bound exciton which can then dissociate, by absorbing a photon or phonon, leading to the generation of free carriers [52], with an associated activation energy E_{BT} [53], as illustrated in Fig. 6(a).

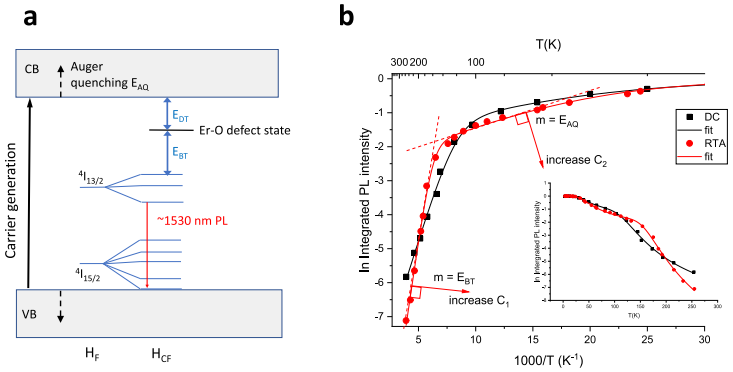

Fig. 6. (a) Standard energy level model for Er:Si illustrating (not to scale) the free ion splitting, H_F, and crystal field splitting, H_{CF}, of Er along with the defect state and possible quenching mechanisms. (b) Arrhenius plot of the temperature dependence of the Er^{3+} integrated PL intensity with 450 nm excitation for DC 950 (black) and RTA 950 (red). Lines describe fits using Eq. 5. Inset is the normalized intensity Vs temperature data for the same samples

Figure 6(b) shows the Arrhenius plot of the temperature dependence of the integrated PL intensity from DC 950 and RTA 950. The general dependence is typical for that observed from Er:Si [9,54–57] with a shallow slope at low temperature which transitions to a steeper slope at higher temperatures. This has been attributed to Auger quenching (at lower T) and (thermally assisted) back transfer (at higher T). These thermal quenching mechanisms are represented in Eq. (5) with E_{BT}, E_{AQ} and their associated pre-factors (C_1, C_2). We fitted the temperature dependence with Eq. (5), as shown in Fig. 6(b), and the fit parameters are shown in Table 4. E_{AQ} is similar to that observed previously [58], while E_{BT} was previously reported to be 150 meV [53]. We find E_{BT} is 200 meV and 90 meV for RTA 950 and DC 950, respectively. The position of the defect state is relevant for photonic applications such as telecoms wavelength Si LEDs and detectors since their operation is via the defect state. Since this defect state is assumed to be related to O impurities around the Er center, the difference in E_{BT} is explained by the different O coordination expected for RTA 950 and DC 950, and implies that increased O coordination pushes the defect level towards the conduction band edge. The fact that $C_2 << C_1$ indicates that Auger is mostly ineffective in quenching, compared with the back transfer process.

$$I(T) = I_0 \frac{1}{1 + C_1 e^{(-E_{BT}/k_B T)} + C_2 e^{(-E_{AQ}/k_B T)}} \tag{5}$$

The n-type conductivity of Er:Si has been related to the presence of the Er-O defect state [59]. However, despite the significant difference in the position of the defect state for DC 950 and

Optics EXPRESS

Table 4. Fitting parameters for temperature dependence of integrated Er^{3+} PL intensity

	RTA 950	DC 950
C_1	1.16E7 ± 3E6	25584 ± 5500
E_{BT} (meV)	198.5 ± 4.8	93.3 ± 3.4
C_2	13.5 ± 1.5	5.8 ± 1.8
E_{AQ} (meV)	12.5 ± 0.8	9.9 ± 1.9

RTA 950 annealing, derived from Fig. 6(b), resistivity measurements in Supplement 1 section S7 show no significant difference between the DC and RTA annealed samples. Additionally, we observed an increase in resistivity, by a factor of three, when the temperature for RTA annealing increased from 700 to 900 °C. Since crystallinity is not fully recovered for samples annealed at lower temperatures, as confirmed by Raman measurements of the 700 and 800 °C RTA samples, this suggests that electrical conductivity may in fact be facilitated by defects, such as O and dislocations, in the crystal lattice, rather than via the optically active Er-O center, in a fully recrystallized lattice. Any conductivity, either due to O centers, dislocations or the Er-O defect, is unfavorable for quantum networking applications because free carriers could increase the propagation loss of Er:Si waveguides, via free carrier absorption (FCA). Supplement 1 section S8 shows PL decay profiles of RTA 950 and DC 950 are both non-exponential with 1/e folding times of ~310 µs and ~710 µs, respectively, indicating different non-radiative decay mechanisms, such as quenching induced by free carriers from the excitation laser, [60] associated with the Er centers in these samples.

4. Conclusions

By increasing the quenching rate of the thermal anneal of Er and O co-implanted Si, using our 'deep cooling' method we change the dominant Er center from Er_2O_3 clusters to a less energetically favorable center with mixed Si and O coordination. We use a variable modulation frequency method to separate peaks belonging to different Er centers in Er:Si with different PL lifetimes.

We show that the spectra of various Er centers can be arranged in a sequence. By fitting CFPs we validate the existence of this sequence and show that the symmetry of these centers is C_{2V}, or lower. By calculating g-factors from the fitted CFPs, we validate the fit. From comparisons to EXAFS measurements, we propose that all Er centers in Er:Si can be arranged in a sequence, ranging from entirely Si coordinated, through mixed Si and O coordination, to entirely O coordinated. Er centers with higher O coordination have an associated O-related defect state which allows indirect excitation.

Future quantum networking applications of Er:Si will require the implantation of Er into high purity SOI; however, studies to date indicate that this results in the formation of four different Er centers. O-coordination of Er is energetically favorable, and a low concentration of O is likely to be unavoidable in SOI, as a result of O diffusion into the thin Si device layer, during the thermal oxidation step of SOI fabrication. We propose that the best case for quantum networking applications is the formation of only the 'Gritsch A' (i.e., Si-coordinated Er) center, since this would avoid excess decoherence and propagation loss associated with other centers, in particular, those with higher O coordination and an O related defect state. The 'deep cooling' process we have devised can push the Er center towards this preferable higher Si coordination state, despite it being energetically less favorable under more conventional thermal annealing cycles. This is likely to be helpful in obtaining only the Gritsch A center for quantum networking applications of Er:Si.

Optics EXPRESS

Funding. Engineering and Physical Sciences Research Council (EP/R011885/1).

Disclosures. The authors declare no conflicts of interest.

Data availability. The datasets generated during the current study are available in the Mendeley Data repository [61].

Supplemental document. See Supplement 1 for supporting content.

References

1. M. P. Hedges, J. J. Longdell, Y. Li, *et al.*, "Efficient quantum memory for light," Nature **465**(7301), 1052–1056 (2010).
2. A. Gritsch, L. Weiss, J. Früh, *et al.*, "Narrow Optical Transitions in Erbium-Implanted Silicon Waveguides," Phys. Rev. X **12**(4), 041009 (2022).
3. M. A. Hughes, N. A. Panjwani, M. Urdampilleta, *et al.*, "Spin echo from erbium implanted silicon," Appl. Phys. Lett. **118**(19), 194001 (2021).
4. I. R. Berkman, A. Lyasota, G. G. de Boo, *et al.*, "Millisecond electron spin coherence time for erbium ions in silicon," arXiv (2023).
5. A. Gritsch, A. Ulanowski, and A. Reiserer, "Purcell enhancement of single-photon emitters in silicon," Optica **10**(6), 783–789 (2023).
6. M. A. Hughes, N. A. Panjwani, M. Urdampilleta, *et al.*, "Coupling of Erbium-Implanted Silicon to a Superconducting Resonator," Phys. Rev. Appl. **16**(3), 034006 (2021).
7. J. D. Carey, J. F. Donegan, R. C. Barklie, *et al.*, "Electron paramagnetic resonance of erbium doped silicon," Appl. Phys. Lett. **69**(25), 3854–3856 (1996).
8. J. D. Carey, R. C. Barklie, J. F. Donegan, *et al.*, "Electron paramagnetic resonance and photoluminescence study of Er-impurity complexes in Si," Phys. Rev. B **59**(4), 2773–2782 (1999).
9. H. Przybylinska, W. Jantsch, Y. Suprun-Belevitch, *et al.*, "Optically active erbium centers in silicon," Phys. Rev. B **54**(4), 2532–2547 (1996).
10. N. Q. Vinh, H. Przybylińska, Z. F. Krasil'nik, *et al.*, "Optical properties of a single type of optically active center in Si/Si:Er nanostructures," Phys. Rev. B **70**(11), 115332 (2004).
11. D. Thao, C. Ammerlaan, and T. Gregorkiewicz, "Photoluminescence of erbium-doped silicon: Excitation power and temperature dependence," J. Appl. Phys. (Melville, NY, U. S.) **88**(3), 1443–1455 (2000).
12. H. Wen, J. He, J. Hong, *et al.*, "Efficient Er/O-doped silicon light-emitting diodes at communication wavelength by deep cooling," Adv. Opt. Mater. **8**(18), 2000720 (2020).
13. P. Zhang, J. Hong, H. Wen, *et al.*, "Fluorescence optimization and ratiometric thermometry of near-infrared emission in erbium/oxygen-doped crystalline silicon," J. Lumin. **250**, 119035 (2022).
14. X. Wang, J. He, A. Wang, *et al.*, "Analytical Impact-Excitation Theory of Er/O/B Codoped Si Light-Emitting Diodes," Phys. Rev. Lett. **132**(24), 246901 (2024).
15. J. Hong, H. Wen, J. He, *et al.*, "Stimulated emission at 1.54 μm from erbium/oxygen-doped silicon-based light-emitting diodes," Photonics Res. **9**(5), 714–721 (2021).
16. M. Lourenço, M. Milošević, A. Gorin, *et al.*, "Super-enhancement of 1.54 μm emission from erbium codoped with oxygen in silicon-on-insulator," Sci. Rep. **6**(1), 37501 (2016).
17. U. Walter, "Treating crystal field parameters in lower than cubic symmetries," J. Phys. Chem. Solids **45**(4), 401–408 (1984).
18. M. A. Hughes, M. A. Lourenço, J. D. Carey, *et al.*, "Crystal field analysis of Dy and Tm implanted silicon for photonic and quantum technologies," Opt. Express **22**(24), 29292–29303 (2014).
19. W. Carnall, G. Goodman, K. Rajnak, *et al.*, "A systematic analysis of the spectra of the lanthanides doped into single crystal LaF_3," J. Chem. Phys. **90**(7), 3443–3457 (1989).
20. A. Abragam and B. Bleaney, *Electron Paramagnetic Resonance of Transition Ions* (1970).
21. M. A. Hughes, R. J. Curry, and D. W. Hewak, "Spectroscopy of titanium-doped gallium lanthanum sulfide glass," J. Opt. Soc. Am. B **25**(9), 1458–1465 (2008).
22. M. A. Hughes, R. J. Curry, and D. W. Hewak, "Determination of the oxidation state and coordination of a vanadium doped chalcogenide glass," Opt. Mater. (Amsterdam, Neth.) **33**(3), 315–322 (2011).
23. Y. Tang, K. Heasman, W. Gillin, *et al.*, "Characteristics of rare-earth element erbium implanted in silicon," Appl. Phys. Lett. **55**(5), 432–433 (1989).
24. K. Nakashima, O. Eryu, H. Akiyama, *et al.*, "Correlation between Er-luminescent centers and defects in Si co-implanted with Er and O," Nucl. Instrum. Methods Phys. Res., Sect. B **175-177**, 208–213 (2001).
25. J. Palm, F. Gan, B. Zheng, *et al.*, "Electroluminescence of erbium-doped silicon," Phys. Rev. B **54**(24), 17603–17615 (1996).
26. J. Michel, J. Benton, R. Ferrante, *et al.*, "Impurity enhancement of the 1.54-μm Er^{3+} luminescence in silicon," J. Appl. Phys. (Melville, NY, U. S.) **70**(5), 2672–2678 (1991).
27. W. Jantsch, H. Przybylinska, C. Skierbiszewski, *et al.*, "Factors Governing the Photoluminescence Yield of Erbium Implanted Silicon," Mater. Res. Soc. Symp. Proc. **422**, 101 (1996).
28. T. Taskin, S. Gardelis, J. Evans, *et al.*, "Sharp 1.54 μm luminescence from porous erbium implanted silicon," Electron. Lett. **31**(24), 2132–2133 (1995).

Optics EXPRESS

29. J. Michel, L. C. Kimerling, J. Benton, *et al.*, "Dopant Enhancement of the 1.54 μm Emission of Erbium Implanted in Silicon," Mater. Sci. Forum **83-87**, 653–658 (1992).
30. K. R. Lea, M. J. M. Leask, and W. P. Wolf, "The raising of angular momentum degeneracy of f-Electron terms by cubic crystal fields," J. Phys. Chem. Solids **23**(10), 1381–1405 (1962).
31. G. F. Koster, *Properties of the Thirty-two Point Groups* (MIT Press, 1963).
32. S. Laachir, M. Moussetad, and R. Adhiri, "Crystal-Field energy levels of trivalent Erbium ion in cubic symmetry," Zeitschrift für Naturforschung A **66**(6-7), 457–460 (2011).
33. M. A. Hughes, H. Li, N. Theodoropoulou, *et al.*, "Optically modulated magnetic resonance of erbium implanted silicon," Sci. Rep. **9**(1), 19031 (2019).
34. Y. Huang, M. Mortier, and F. Auzel, "Stark levels analysis for Er^{3+}-doped oxide glasses: germanate and silicate," Opt. Mater. (Amsterdam, Neth.) **15**(4), 243–260 (2001).
35. P. H. Butler, *Point Group Symmetry Applications: Methods and Tables* (Springer Science & Business Media, 2012).
36. J. B. Gruber, J. Henderson, M. Muramoto, *et al.*, "Energy levels of single-crystal erbium oxide," J. Chem. Phys. **45**(2), 477–482 (1966).
37. J. B. Gruber, R. P. Leavitt, C. A. Morrison, *et al.*, "Optical spectra, energy levels, and crystal-field analysis of tripositive rare-earth ions in Y_2O_3. IV C3i sites," J. Chem. Phys. **82**(12), 5373–5378 (1985).
38. A. Barcz, "Silicon Dioxide as a Boundary for Oxygen Outdiffusion from CZ-Si," Defect Diffus. Forum **297-301**, 688–693 (2010).
39. A. Barcz, A. Panas, and R. Jakiela, "Out-and in-diffusion of oxygen ^{16}O in silicon," Semicond. Sci. Technol. **19**(11), 1311–1314 (2004).
40. T. Abe and H. Yamada-Kaneta, "Annealing behavior of oxygen in-diffusion from SiO_2 film to silicon substrate," J. Appl. Phys. (Melville, NY, U. S.) **96**(8), 4143–4149 (2004).
41. N. Vinh, H. Przybylińska, Z. Krasil'nik, *et al.*, "Observation of Zeeman effect in photoluminescence of Er^{3+} ion imbedded in crystalline silicon," Phys. B **308-310**, 340–343 (2001).
42. F. d'Acapito, S. Mobilio, S. Scalese, *et al.*, "Structure of Er-O complexes in crystalline Si," Phys. Rev. B **69**(15), 153310 (2004).
43. N. Theoropoulou, *Optical and Electrical Characteristics of Erbium Doped Solids for Quantum Technology Applications* (University of Salford, 2023).
44. D. L. Adler, D. C. Jacobson, D. J. Eaglesham, *et al.*, "Local structure of 1.54 μm luminescence Er^{3+} implanted in Si," Appl. Phys. Lett. **61**(18), 2181–2183 (1992).
45. A. Terrasi, F. Priolo, G. Franzo, *et al.*, "EXAFS analysis of Er sites in Er–O and Er–F co-doped crystalline Si," J. Lumin. **80**(1-4), 363–367 (1998).
46. A. Terrasi, G. Franzò, S. Coffa, *et al.*, "Evolution of the local environment around Er upon thermal annealing in Er and O co-implanted Si," Appl. Phys. Lett. **70**(13), 1712–1714 (1997).
47. D. Prezzi, T. Eberlein, R. Jones, *et al.*, "Electrical activity of Er and Er-O centers in silicon," Phys. Rev. B **71**(24), 245203 (2005).
48. S. Rinner, F. Burger, A. Gritsch, *et al.*, "Erbium emitters in commercially fabricated nanophotonic silicon waveguides," Nanophotonics **12**(17), 3455–3462 (2023).
49. J. D. Carey, R. C. Barklie, J. F. Donegan, *et al.*, "EPR study of erbium-impurity complexes in silicon," J. Lumin. **80**(1-4), 297–301 (1998).
50. J. Yang, W. Fan, Y. Zhang, *et al.*, "Zeeman and hyperfine interactions of a single $^{167}Er^{3+}$ ion in Si," Phys. Rev. B **105**(23), 235306 (2022).
51. G. Schäfer and S. Scheller, "Paramagnetische Resonanz von Er^{3+} in Y_2O_3," Eur. Phys. J. B **5**(1), 48–57 (1966).
52. A. Polman, "Erbium as a probe of everything?" Phys. B (Amsterdam, Neth.) **300**(1-4), 78–90 (2001).
53. A. J. Kenyon, "Erbium in silicon," Semicond. Sci. Technol. **20**(12), R65–R84 (2005).
54. N. Hamelin, P. G. Kik, J. F. Suyver, *et al.*, "Energy backtransfer and infrared photoresponse in erbium-doped silicon p–n diodes," J. Appl. Phys. (Melville, NY, U. S.) **88**(9), 5381–5387 (2000).
55. A. Polman, "Erbium implanted thin film photonic materials," J. Appl. Phys. (Melville, NY, U. S.) **82**(1), 1–39 (1997).
56. G. Van den Hoven, J. H. Shin, A. Polman, *et al.*, "Erbium in oxygen-doped silicon: Optical excitation," J. Appl. Phys. (Melville, NY, U. S.) **78**(4), 2642–2650 (1995).
57. F. Priolo, G. Franzò, S. Coffa, *et al.*, "The erbium-impurity interaction and its effects on the 1.54 μm luminescence of Er^{3+} in crystalline silicon," J. Appl. Phys. (Melville, NY, U. S.) **78**(6), 3874–3882 (1995).
58. F. Priolo, G. Franzò, S. Coffa, *et al.*, "Excitation and nonradiative deexcitation processes of Er^{3+} in crystalline Si," Phys. Rev. B **57**(8), 4443–4455 (1998).
59. L. Palmetshofer, Y. Suprun-Belevich, and M. Stepikhova, "Donor activity of ion-implanted erbium in silicon," Nucl. Instrum. Methods Phys. Res., Sect. B **127-128**, 479–482 (1997).
60. N. Vinh, S. Minissale, B. Andreev, *et al.*, "The Auger process of luminescence quenching in Si/Si: Er multinanolayers," J. Phys.: Condens. Matter **17**(22), S2191–S2195 (2005).
61. M. Hughes, "Hughes deep cooling," Mendeley Data (2024), https://data.mendeley.com/datasets/k9ccfgh3pb/1.